CRYSTAL Research & Technology

Cryst. Res. Technol. 51, No. 10, 634–644 (2016) / DOI 10.1002/crat.201600227

Original Paper

On the morphology of $BaMoO_4$ crystals: A theoretical and experimental approach

Marisa C. Oliveira[1,2], Lourdes Gracia[1], Içamira C. Nogueira[3], Maria Fernanda C. Gurgel[4], Jose Manuel R. Mercury[5], Elson Longo[2], and Juan Andrés[1,]*

Received 18 July 2016, revised 4 August 2016, accepted 15 August 2016
Published online 8 September 2016

$BaMoO_4$ crystals were obtained by a co-precipitation method, and their structures were characterized by X-ray diffraction and Rietveld refinement techniques. Field emission scanning electron microscopy was utilized to investigate the morphology of the as-synthesized aggregates.- Through systematic first principle calculations within the density functional theory method at the B3LYP level, we investigated the structure; the surface stability of the (001), (101), (110), (100), (111), and (112) surfaces; and the morphological transformations of $BaMoO_4$. The relative surfaces energies were further varied to predict a complete map of the available morphologies through a Wulff construction approach. This revealed that the obtained experimental and theoretical morphologies coincided when the surface energy values of the (001) surface decreased while those of the (100) and (101) facets increased simultaneously. Analysis of the surface structures showed that the electronic properties were associated with the presence of undercoordinated $[BaO_x]$ ($x = 4$, 5, and 6) and $[MoO_y]$ ($y = 3$) clusters. The presented results provide a comprehensive catalog of the morphologies most likely to be present under realistic conditions, and will serve as a starting point for future studies on the surface chemistry of $BaMoO_4$ crystals.

1 Introduction

Barium molybdate ($BaMoO_4$) is a prototypical member of the molybdate family with a scheelite-type tetragonal structure. This compound has been prepared by a plethora of synthetic routes including solid-state reactions, Czochralski techniques, spontaneous crystallization, microwave-assisted synthesis, hydrothermal synthesis, co-precipitation, microemulsion, and complex polymerization. [1–15] Of these procedures, co-precipitation has been demonstrated to be one of the most effective approaches to synthesize inorganic compounds with interesting morphologies and regular particle size. [16–23].

The morphology of a given material is related to the stability of their various corresponding exposed surfaces, which can be rigorously described by their surface energies. In this context, first principle calculations have been gradually developed and employed for the study of crystal morphology. This has enabled the understanding of the atomic and electronic properties of a crystal surface, which has provided some insight into the features of single crystal facets relevant to subsequent technological applications. [24, 25] In particular, these applications for $BaMoO_4$ can be further enhanced or optimized by tailoring the surface atomic structures. [26–28].

It is well known that the morphologies of $BaMoO_4$ are sensitive to the synthesis conditions, and a number of different shapes of $BaMoO_4$ crystals have been synthesized and studied such as penniform-like, [29] flower-like, [30] nest-like, [31] and shuttle-like [32, 33] shapes. Our group are engaged in a research project devoted to developed and apply a working methodology, based on the joint use of experimental findings and first-principles calculations, to obtain the electronic, structural and energetic properties controlling

* Corresponding author: e-mail: andres@qfa.uji.es
[1] Departament de Química Física i Analítica, Universitat Jaume I, 12071 Castelló de la Plana, Spain
[2] CDMF-UFSCar, Universidade Federal de São Carlos, P.O. Box 676, 13565-905, São Carlos, SP, Brazil
[3] Departament de Física, Universidade Federal do Amazonas, 69077–000, Manaus, AM, Brazil
[4] Department de Química, Universidade Federal de Goiás, 75704-020, Catalão, GO, Brazil
[5] PPGEM-IFMA, Instituto Federal do Maranhão, 65030-005, São Luís, MA, Brazil

CRYSTAL Research & Technology

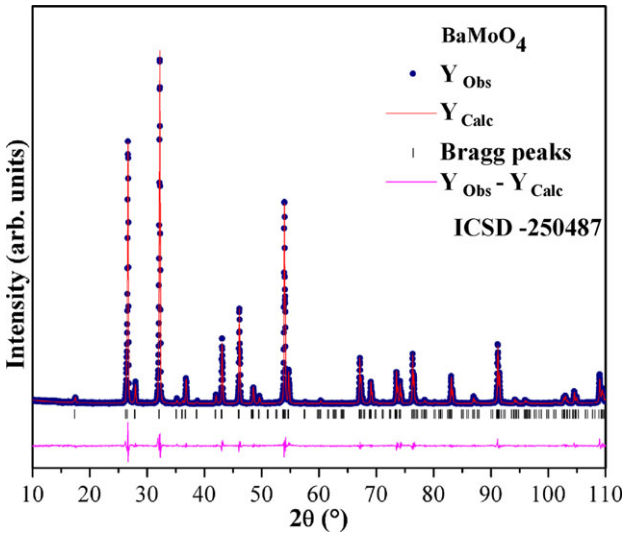

Fig. 1 Rietveld refinements of the $BaMoO_4$ crystals synthesized at 80 °C using the co-precipitation method.), XRD pattern using Cu Kα radiation ($\lambda = 1.5406$ Å) in a 2θ range from 10° to 110°.

the morphology and the transformation mechanism of complex crystals. Very recently this strategy has been used in $BaWO_4$ crystals. [34] This work follows a joint experimental and theoretical strategy on another scheelite based material, $BaMoO_4$ crystals, to obtain a complete map of the morphologies available for this material. In addition, based on these results, we are able to rationalize how the different surfaces change their energies throughout the synthesis process, and we are able to propose the path by which the experimental and theoretical morphologies of $BaMoO_4$ can match.

This paper is divided into three sections. Next, our results are presented and discussed and our main conclusions. Next, our results the experimental details and the computational model and method used, are summarized in the final section.

2 Results and discussion

2.1 X-Ray diffraction measurements and Rietveld refinements

Figure 1 shows the Rietveld refinement plots for the observed patterns versus the calculated patterns of the $BaMoO_4$ crystals obtained using a co-precipitation method.

The measured diffraction patterns were well adjusted to the ICSD N°. 250487. [35] All the diffraction peaks can be readily indexed to the pure scheelite-type tetragonal structure of $BaMoO_4$ (space group: $I4_1/a$). No additional phase peaks were observed in the resolution range, indicating that the pure tetragonal phase $BaMoO_4$ can be obtained. The strong and sharp diffraction peaks suggested the synthesized crystals were well-crystallized. To confirm that the structure of the $BaMoO_4$ crystals was tetragonal and to determine the lattice parameters, cell volume, and atomic coordinates, a structural refinement using the Rietveld method was performed for the $BaMoO_4$ crystals.

The quality of the structural refinement was checked using the statistical parameters R_{wp}, R_{Bragg}, R_p, and χ^2 (12.50%, 5.78%, 8.67% and 1.36%, respectively). The low deviations of these parameters, which indicates the good quality of the structural refinement and numerical results. A previous work, including structural refinement data, showed that all the $(Ba_{1-x}Sr_x)MoO_4$ crystals were crystallized in a scheelite-type tetragonal structure with the $I4_1/a$ space group, and four molecular formula per unit-cell ($Z = 4$). [35] Our results (a, $b = 5.5830(9)$ Å, $c = 12.8270(7)$ Å) closely agree with the lattice parameters reported for $x = 0$ of the solid solution, namely a, $b = 5.58483(2)$ Å, $c = 12.82922(9)$ Å. Variations in the atomic coordinates related to oxygen atoms were observed in Table 1. This is possible because the Ba and Mo positions were fixed by the crystal symmetry and only the atomic positions for oxygen were refined. [36].

Figure 2 illustrates a schematic representation of a single conventional $1\times1\times1$ cell for $BaMoO_4$. The lattice parameters and atomic positions were confirmed using Rietveld refinement to model this unit cell. In terms of cluster organization, the Mo atoms are surrounded by four oxygen atoms $[MoO_4]$ in a tetrahedral configuration and Ba atoms are surrounded by eight oxygen atoms in a deltahedral configuration $[BaO_8]$. [8].

For comparison purposes, the calculated and experimental values of the lattice parameters (a and c) and the atomic coordinates of the oxygen atoms are presented in Table 1.

These results are in good agreement with previous experimental observations and calculations. [14, 35, 37–44]. In addition, theoretical and experimental results can be compared with previous studies of other scheelite-type materials, [45, 46] where the calculations describe precisely the evolution of the crystal structure on pressure phases and help to understand the electronic and structural properties.

2.2 Surface study

The surface energy values, E_{surf}, for (001), (101), (110), (100), (111), and (112) surfaces were calculated in order to correlate the theoretical and experimental studies.

Table 1 Calculated and experimental values of the lattice parameters (a and c) and atomic coordinates x, y, z of the oxygen.

	Cell parameters		Oxygen coordinates		
Data	a (Å)	c (Å)	x	y	z
Theo. (this work)	5.5927	12.4055	0.2311	0.1218	0.0460
Exp. (this work)	5.583(09)	12.827(07)	0.233(29)	0.126(67)	0.057(48)
Exp. [35]	5.5848	12.8292	0.2283	0.1353	0.0489
Theo [37, 38]	5.5364	12.7153	-	-	-
Exp. [39]	5.5479	12.7432	-	-	-
Exp. [40]	5.5622	12.8188	-	-	-
Exp. [41, 42]	5.5877	12.8067	-	-	-
Exp. [43]	5.573	12.786	-	-	-
Exp. [44]	5.580	12.810	-	-	-
Ep. [14]	5.5802	12.821	-	-	-
Interatomic distance(˚A)	Calculated		Experimental		Difference
Ba-O	2.7249		2.718(40)		−0.006
Ba-O	2.7610		2.848(42)		0.087
Mo-O	1.7855		1.708(97)		−0.076

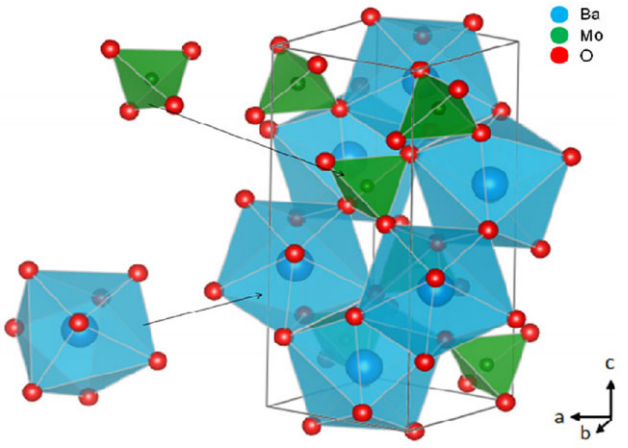

Fig. 2 A polyhedral representation of the BaMoO4 unit cell. The local coordination corresponding to the deltahedral [BaO_8] and tetrahedral [MoO_4] clusters is depicted for both the Ba and Mo atoms, respectively.

Surface energy is defined as the energy per unit area required for forming the surface relative to the bulk and is calculated according to:

$$E_{surf} = \frac{E_{slab} - nE_{bulk}}{2A}$$

where E_{slab} is the total energy of the 2D slab, nE_{bulk} is the energy of the corresponding amount of the bulk $BaMoO_4$ units, and A represents the surface area, which is created on each side of the 2D slab and is repeated periodically. After the corresponding optimization process and convergence tests in thickness, slab models consisting of four molecular units containing 24 atoms were obtained. All these surfaces are presented in figure 3 with the coordination number, i.e., clusters of the most exposed Ba and Mo atoms.

Considering the surface atom distributions, we note that the surfaces (101), (111), and (112) are exposed to a vacuum by the Mo and O atoms, while the (001), (100), and (110) surfaces are exposed by the Ba and O atoms. Exposed Mo atoms can be coordinated to three or four oxygen atoms, forming [MoO_3] or [MoO_4] clusters, respectively. Exposed Ba atoms can be coordinated to four, five, or six oxygen atoms, forming [BaO_4], [BaO_5], or [BaO_6] clusters, respectively.

Analysis of the results shows that the most stable surface, the (001) surface, presents exposed [BaO_6] clusters, corresponding to the presence of two oxygen vacancies compared to the bulk. However, in the (100), (110), (101), and (111) surfaces there are undercoordinated [BaO_5] clusters associated to the presence of three oxygen

CRYSTAL Research & Technology

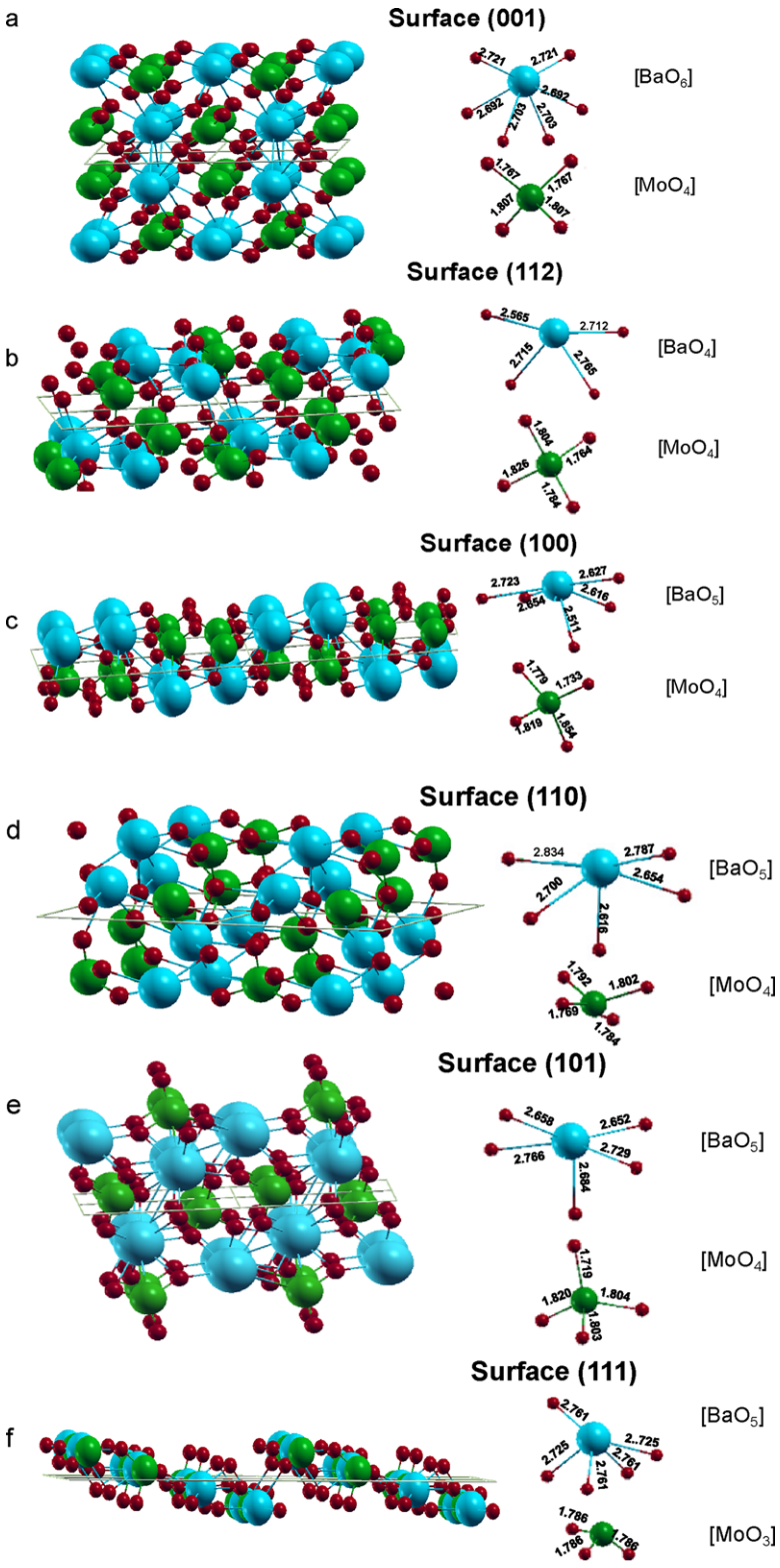

Fig. 3 Schematic representations of surfaces: a) (001), b) (112), c) (100), d) (110), e) (101), and f) (111). The values for the Ba–O and Mo–O bond distances of the exposed Ba and Mo atoms are given in Å.

vacancies. On the (112) surface there are four oxygen vacancies, i.e., undercoordination at [BaO_4]. Only the (111) surface presents [MoO_3] clusters, implying a breaking of a Mo–O bond compared to the bulk. Since the bonding interaction of a Mo–O bond is stronger than a Ba–O bond, the stability of this surface is reduced compared to the rest of the surfaces.

2.3 Morphologies of the $BaMoO_4$ crystals

The conventional approach to the quantitative study of morphology is through the determination of the surface energy of each surface, as defined by the Wulff construction [47–49] using the *ab initio* calculated surface energies. From the Wulff construction, it is derived that the surfaces with the lowest surface energies control the crystal morphology of $BaMoO_4$. [42, 43].

The FE-SEM images of the $BaMoO_4$ crystals synthesized at 80 °C by the co-precipitation method are shown in figure 4. The micro-structured $BaMoO_4$ crystals were obtained immediately after the reaction between the (Ba^{2+}) and (MoO_4^{2-}) ions. The speed of nucleation was very fast.

The $BaMoO_4$ crystals exhibited a large quantity of particles with an agglomerate nature and polydisperse sizes. The particles were of a considerable length with a surface with many notches and well-formed perpendicular branches (see figure 4**).**

The order of the stability of the $BaMoO_4$ surfaces according to the theoretical calculations is (001) > (112) > (100) > (110) > (101) > (111) and the ideal morphology of $BaMoO_4$ is controlled by (001), (112), and (100), being their contribution 15.1%, 70.9%, and 14.0%, respectively. Based on the results of the experimental micrographs (see figure 4), it is possible to modify the ideal morphology by tuning the values for the surface energies of the different facets using the Wulff construction. [47–50] Analysis of the theoretical results showed that when the relative stability of the facets changes (increases or decreases), more than one type of facet will appear in the resulting morphology. The available morphologies reflecting a change in the values of the surface energy, i.e., modifying the stability of the surfaces to generate the corresponding morphology, are depicted in figure 5. In order to obtain a similar morphology to the experimental FE-SEM images, the values of the surface energy for the (001) were increased and the surface energy for (100) and (101) decreases, simultaneously (see right-hand side of figure 5).

Recently, Gao et al. [51] reported that the surfaces of scheelite crystal have predominantly exposed surfaces, (001), (112), and (100) in the morphologies, with the (112) crystal surface as the most commonly exposed surface. [52–54] This result is in agreement with present result our and whose obtained in the previous study on $BaWO_4$. [34] A comparison between $BaWO_4$ and $BaMoO_4$ shows that ideal morphology of both scheelites is similar. However, the experimental FE-SEM images are different for both materials, i.e. 99.5% contribution of (112), 0.4% of (100) and 0.1% of (001) in $BaWO_4$ while 46.5% of (101), 46.9% of (100), 5.8% of (112) and 0.8% of (001) are found for $BaMoO_4$.

Another important aspect that should be considered when studying solid materials is a distinction between the surface energy, E_{surf}, and the surface tension, σ. The surface tension is "surface stress" represented by a work force per unit area in the surface layer. [55, 56] The surface tension can be obtained using the thermodynamic stability model described by the equation $\sigma = \partial E_{tot}/\partial A$, where E_{tot} is the total energy with contributions from the particle bulk and surfaces. To calculate E_{tot}, the uniform dilation with area ΔA (corresponding to a constant ratio between the in-plane lattice parameters, *x*:*y*) of the structure must be calculated while optimizing only the internal parameters (without optimization of the in-plane cell parameters). Thus, E_{tot} can be calculated as $\frac{1}{2}(E_{slab} - nE_{bulk})$ for optimized structures and surfaces after dilation. Therefore, by applying two-dimensional dilation to a slab in the surface plane and calculating the total energy as previously described, a change in the total energy (ΔE_{tot}) after dilation was obtained for a given dilation area. The values for the surface energy and tension are listed in Table 2.

The results collected in Table 2 show that the surface (101) presents a low value of surface tension, consistent with the stability provided by the six-fold coordination of the Ba atom. Evidence of this was only observed for the (001) and (101) surfaces.

Growth in the <001> direction, the most stable surface, can be related to the differences in the surface energy, which can drive the morphology of products with high tropism. The interaction of small particles may have promoted growth of the crystals, forming large microstructures by self-assembly due to Oswald's ripening, because so many notches can be seen on the surface of the crystals. [33, 57, 58].

The surface relaxation energy values, which are associated with concerted layer breathing due to the loss of atomic coordination, can be observed in Table 2. The (112) and (110) surfaces are found to be the most prone to relax. The coordination number of the exposed Ba atom is reduced to the middle, [BaO_4], compared to the bulk in the (112) surface, while the

CRYSTAL Research & Technology

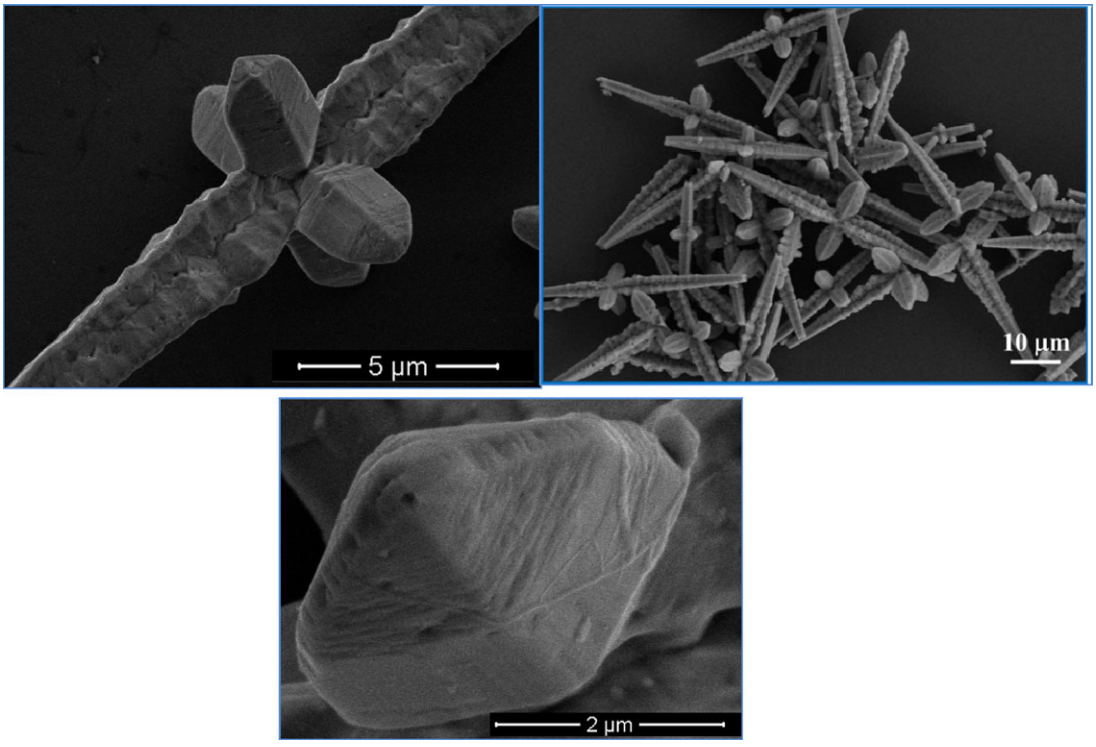

Fig. 4 FE-SEM images of the $BaMoO_4$ crystals.

Table 2 The calculated values of the surface energy, surface tension, change in total energy (ΔE_{tot}) for the area dilation (ΔA), relaxation energy, and gap energy, for each surface.

Surface	E_{suf} (J/m²)	ΔE_{tot} (Hartree)	ΔA (Å²)	σ (J/m²)	Relaxation (%)	E_{gap} (eV)
(001)	0.99	0.035	1.273	0.54	6	5.69
(112)	1.02	0.032	2.385	0.85	62	5.81
(100)	1.17	0.039	2.853	1.04	30	5.38
(110)	1.23	0.033	2.017	1.01	61	5.63
(101)	1.34	0.039	1.562	0.94	37	5.09
(111)	2.23	0.016	4.231	2.51	1	Conductor

$[BaO_5]$ cluster has the longest Ba–O distance (2.834 Å) in (110).

2.4 Band structure for the $BaMoO_4$ bulk and surfaces

The band structures of the $BaMoO_4$ were calculated for 80 k-points along the appropriate high-symmetry paths of the adequate Brillouin zone. Diagrams of the density of state (DOS) were obtained analysis of the corresponding electronic structures shown in figure 6.

The calculated band structure and total DOS projected on atoms for the (001), (112), (100), (110), (101), and (111) surfaces and the bulk $BaMoO_4$ crystal are shown in figure 6 (a–g). It can be easily seen that the upper valence band is composed predominantly of the O 2p states and the bottom of conduction band is mainly attributed to the Mo 4d states and the O 2p states. Based on the literature, AMO_4 oxides with a scheelite structure, such as $BaMoO_4$, contain an M cation exhibiting the closest valence to the nominal value of 6+, showing the covalent property of the crystals, which is mainly contributed by the Mo–O bond. [39].

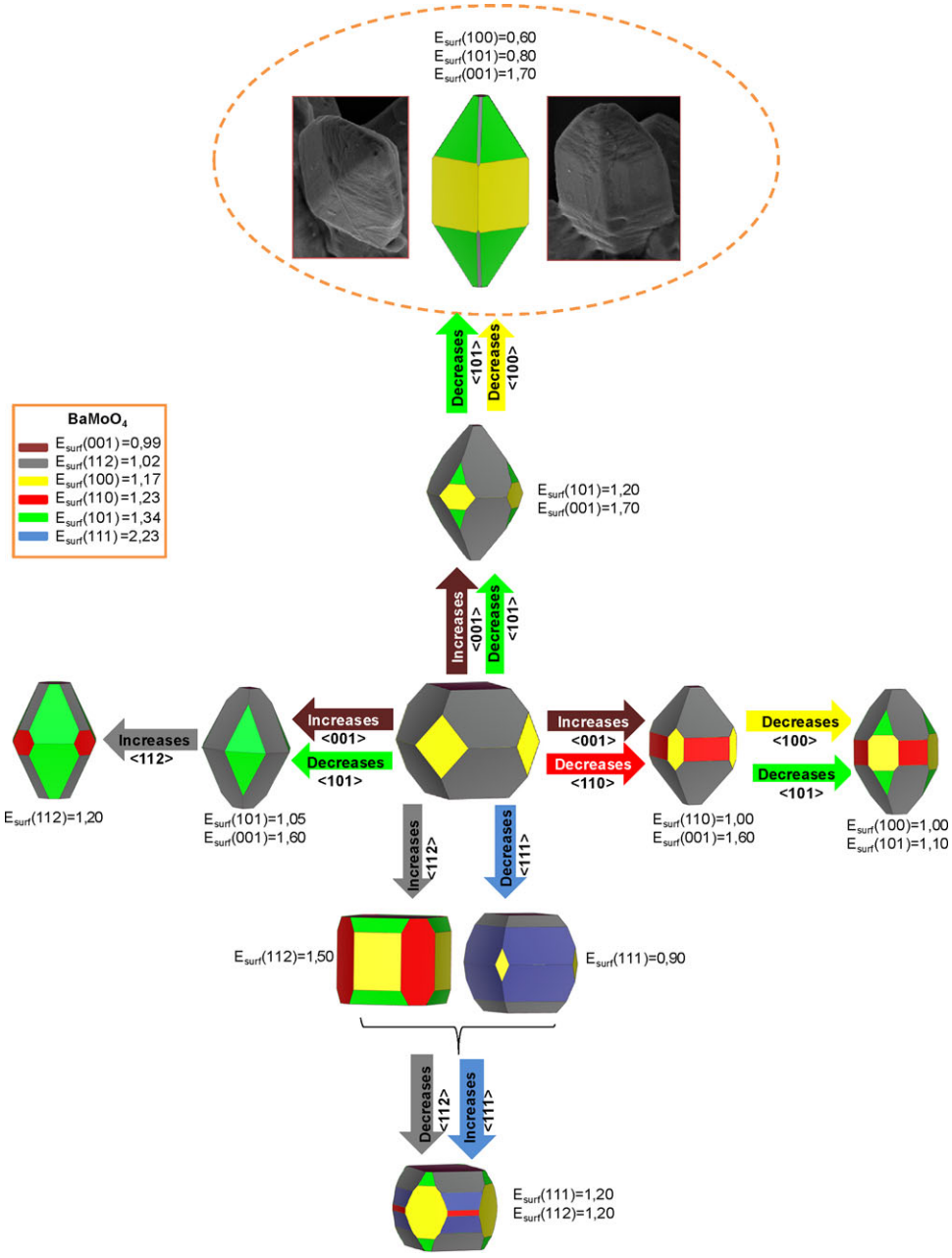

Fig. 5 Crystallographic structures and morphology map for the $BaMoO_4$ crystals (the surface energy units are given in J/m^2). The experimental FE-SEM images (inset) are included for comparison.

In relation to the band structures, the differences in the structural properties of the bulk and the surfaces can be observed. This is due to the reduced coordination of the O atoms in the top layers, which causes spacing between the adjacent layers due to vacancies. The coordination numbers for the exposed metal atoms are presented in figure 3. The essential features of the different surfaces remain constant but significant differences in the distribution of the electronic states is observed for the (001), (100), (110), and (101) surfaces, where the reduced coordination environment of the surface terminated oxygen atoms gives rise to a split-off feature in the O 2p and Mo 4d partial DOS at the bottom of the conduction band. Surface states reduce the bulk band gap (5.8 eV) by 0.1–0.7 eV depending on the specific surface, as can be observed in Table 2. At this stage, a note of caution is mandatory, it is well known that DFT approach underestimates the band gap energy due to its

CRYSTAL Research & Technology

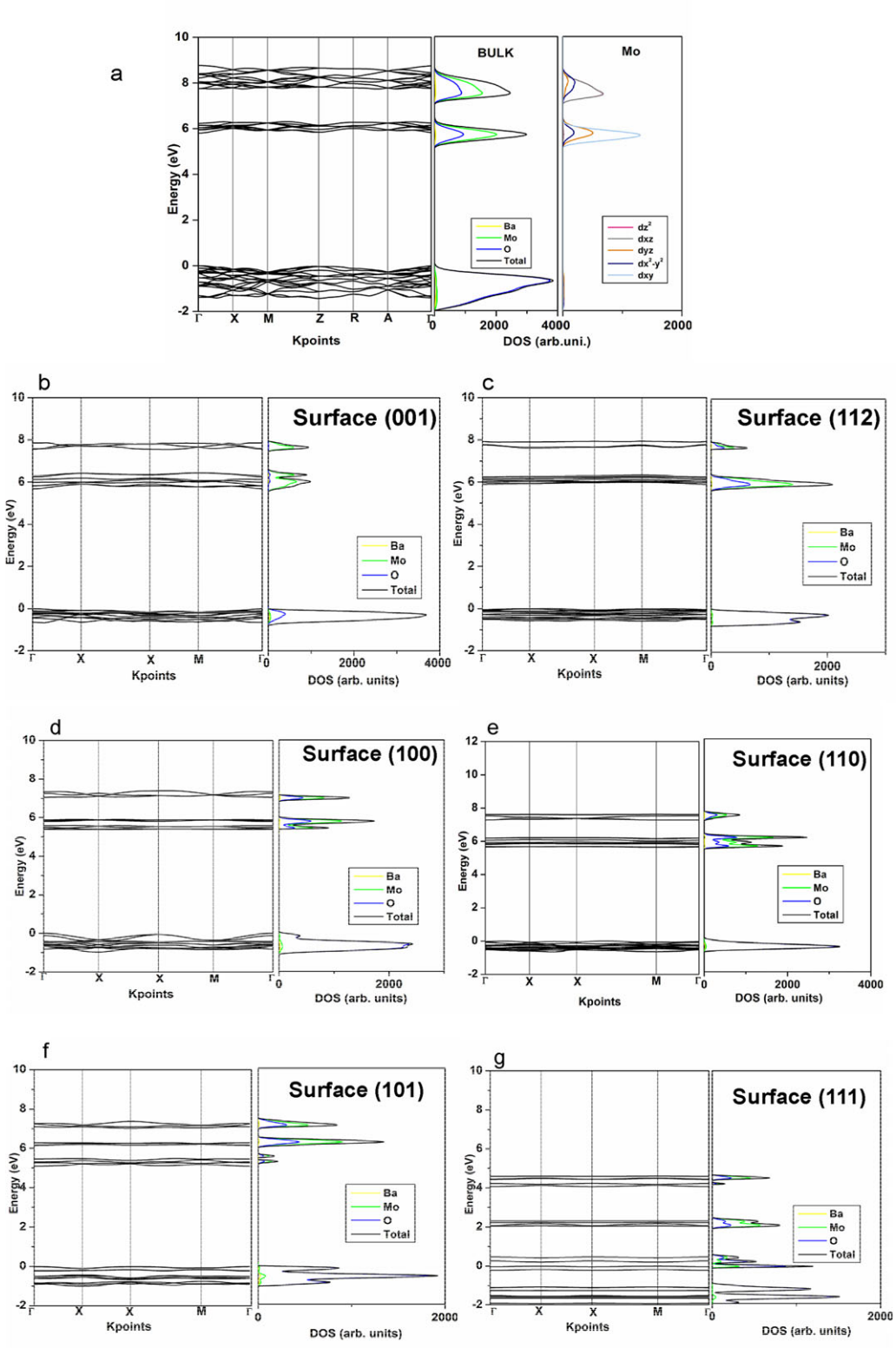

Fig. 6 Calculated band structures and DOS for (a) bulk $BaMoO_4$ and the (b) (001), (c) (112), (d) (100), (e) (110), (f) (101), and (g) (112) surfaces.

independent particle picture. [59–62] All surfaces present an insulating band gap except for the (111) surface, which has a large surface energy value and exhibits a conducting behavior. This can be attributed to the three oxygen vacancies in the undercoordinated [BaO_5] cluster and one of them in [MoO_3] cluster, being the Mo-O interaction more covalent than Ba–O interaction. This result is similar than in scheelite $BaWO_4$ system. [34].

3 Conclusion

Systematic DFT calculations were carried out to study the structure, surface stability (involving the (001), (101), (110), (100), (111), and (112) surfaces), and morphological transformations of $BaMoO_4$. The experimental simulations complemented the FE-SEM techniques used to investigate the morphology of the as-synthesized $BaMoO_4$ aggregates.

The main conclusions of this work can be summarized as follows. i) A simple preparation route using a co-precipitation method can provide an effective process to synthesize inorganic compounds with interesting morphologies and regular particle sizes with an easy handling process and a short reaction time. ii) The building blocks of the $BaMoO_4$ structure were deltahedral [BaO_8] and [MoO_4] clusters, i.e., a local coordination structure for both the Ba and Mo atoms. iii) The order of stability of the $BaMoO_4$ surfaces according to theoretical calculations was (001) > (112) > (100) > (110) > (101) > (111). iv) The calculated morphology of the $BaMoO_4$ based on the Wulff construction was (112) (70.9%), (001) (15.1%), and (100) (14.0%) with the (112) crystal surface as the commonly exposed surface. v) The relative energetics of all the surface structures were modulated to obtain a complete map of the morphologies available for $BaMoO_4$, which enabled us to identify where the observed morphology from the FE-SEM images was located on this map. vi) The obtained experimental and theoretical morphologies coincided when the value of the surface energy for the (001) surface decreased while that of the (100) and (101) surfaces simultaneously increased. vi) Analysis of the surface structures suggested that the electronic properties could be associated with the presence of undercoordinated [BaO_x] ($x = 4$, 5, and 6) and [MoO_y] ($y = 3$) clusters. vi) Finally, the present study could serve as an appropriate model to clarify how knowledge about surface-specific properties could be utilized to design crystal morphologies that exhibit improved performances in various applications.

4 Experimental section

Synthesis of the $BaMoO_4$ crystals: $BaMoO_4$ crystals were synthesized by a simple co-precipitation route at 80 °C. All chemical reagents were of analytical grade and were used without further treatment. Sodium molybdate dihydrate (1×10^{-3} mol) ($Na_2MoO_4.2H_2O$, Strem Chemicals, 99.95%) was dissolved in 50 mL of distilled water at 80 °C with vigorous stirring. Then, barium nitrate (1×10^{-3} mol) ($Ba(NO_3)_2$, Sigma-Aldrich, 99%), solubilized in 50 mL of distilled water at 80 °C, was added under constant stirring. The pH of the solution was maintained at 7, and the temperature was maintained at 80 °C. Then, there was a rapid formation of a white precipitate. This precipitate was washed with distilled water several times. Finally, it was collected and dried in a conventional furnace at 323 K for 8 h.

Characterization of the $BaMoO_4$: The phase composition of the as-prepared sample was detected by X-ray powder diffraction (XRD, D/MAX/2500PC, Rigaku, Japan), operating at 40 kV and 150 mA, Cu Kα radiation ($\lambda = 1.5406$ Å) in a 2θ range from 10° to 110° with a scan rate of 0.02°/min. Rietveld refinement [63] of the measured XRD pattern was carried out using the general structure analysis (GSAS) program. [64] The diffraction peak profiles were adjusted using the Thompson–Cox–Hastings pseudo-Voigt (pV-TCH) function and by an asymmetry function, as described by Finger et al. [65] The background was corrected using a Chebyschev polynomial of the first order. The strain anisotropy broadening was corrected using the phenomenological model described by Stephens. [66] A field-emission scanning electron microscope (FE-SEM, Inspect F50, FEI Company, Hillsboro, OR) was used to observe the morphology of the particles.

Theoretical Calculations: In this work, we simulated, considering symmetrical slabs (with respect to the mirror plane), the (001), (101), (110), (100), (111), and (112) surfaces of $BaMoO_4$. Morphology studies have been carried out on various metal oxides such as $PbMoO_4$, [67] $CaWO_4$, [68] α-Ag_2WO_4, [24] and Ag_3PO_4, [69] as well as Co_3O_4, Fe_2O_3, In_2O_3, [25] α-Ag_2MoO_4, [70] and $BaWO_4$. [34] All these studies have shown a combination of experimental and theoretical insights into the electronic, structural, and energetic properties controlling the morphology and transformation mechanisms, and the corresponding computational methodology, based on the Wulff construction, can be found in these papers.

The calculations were carried out with the CRYSTAL14 computer program [71] within the framework of the density functional theory (DFT) with the hybrid

functional B3LYP. [72, 73] The atomic centers were described using the basis sets for the Mo [74] pseudopotential, and the O [74] and Ba [75] (6-31G* basis set) were described by the standards, respectively. The Brillouin zone was sampled using the Monkhorst–Pack method and at different k-point grids according to the system size. The thresholds controlling the accuracy of the calculation of the Coulomb and exchange integrals were set to 10^{-8} (ITOL1 to ITOL4) and 10^{-14} (ITOL5), which assures a convergence in total energy better than 10^{-7} a.u., whereas the percentage of Fock/Kohn–Sham matrix mixing was set to 40 (IPMIX = 40). [76].

Acknowledgements. This work was financially supported by the following Spanish research funding institutions: the CTQ2012-36253-C03-02 project (Ministerio de Economia y Competitividad), and the PrometeoII/2014/022 and ACOMP/2014/270 projects (Generalitat Valenciana) and the following Brazilian research funding institutions: CNPq (INCTMN 573636/2008-7), FAPESP (2013/07296-2, 2012/14468-1, 2013/26671-9, and 2014/04350-9), CAPES/PNPD 1268069 (process A104/2013 and 99999.002998/2014-09), and the Programa de Cooperación Científica con Iberoamerica (Brasil) of Ministerio de Educación (PHBP14-00020). J.A. acknowledges the Ministerio de Economia y Competitividad "Salvador Madariaga" program, PRX15/00261.L.G. acknowledges Banco Santander (Becas Iberoamérica: Jóvenes profesores e investigadores). M.C. acknowledges Generalitat Valenciana for the Santiago Grisolia Program 2015/033.

Key words. $BaMoO_4$, co-precipitation method, morphology, Wulff construction.

References

[1] B. Wu, W. Yang, H. Liu, L. Huang, B. Zhao, C. Wang, G. Xu, and Y. Lin, Spectrochim. Acta A. **123**, 12 (2014).
[2] T. T. Basiev, A. A. Sobol, Y. K. Voronko, and P. G. Zverev, Opt. Mater. **15**, 205 (2000).
[3] D. A. Spassky, S. N. Ivanov, V. N. Kolobanov, V. V. Mikhailin, V. N. Zemskov, B. I. Zadneprovski, and L. I. Potkin, Radiat. Meas. **38**, 607 (2004).
[4] C. S. Lim, J. Lumin. **132**, 1774 (2012).
[5] J. H. Ryu, J. W. Yoon, and K. B. Shim, J. Alloys Compd. **413**, 144 (2006).
[6] C. Zhang, L. Zhang, C. Song, G. Jia, S. Huo, and S. Shen, J. Alloy Compd. **589**, 185 (2014).
[7] G. R. Tian and S. X. Sun, Cryst. Res. Technol. **45**, 188 (2010).
[8] M. Ghaed-Amini, M. Bazarganipour, M. Salavati-Niasari, and K. Saberyan, Trans. Nonferrous Met. Soc. China. **25**, 3967 (2015).
[9] W. -L. Feng, Y. Jin, Y. Wu, D. -F. Li, and A. -K. Cai, J. Lumin. **134**, 614 (2013).
[10] Y. Mi, Z. Huang, Z. Zhou, F. Hu, and Q. Meng, Chem. Lett. **38**, 404 (2009).
[11] Y. Sun, J. Ma, J. Fang, C. Gao, and Z. Liu, Ceram. Int., **37**, 683 (2011).
[12] A. P. A. Marques, D. M.A. de Melo, C. A. Paskocimas, P. S. Pizani, M. R. Joya, E. R. Leite, and E. Longo, J. Solid State Chem. **179**, 671 (2006).
[13] M. F. C. Abreu, F. V. Motta, R. C. Lima, M. S. Li, E. Longo, and A. P. de A. Marques, Ceram. Int. **40**, 6719 (2014).
[14] A. Gholami and M. Maddahfar, J. Mater. Sci.: Mater. Electron. **27**, 6773 (2016).
[15] J. C. Sczancoski, L. S. Cavalcante, N. L. Marana, R. O. da Silva, R. L. Tranquilin, M. R. Joya, P. S. Pizani, J. A. Varela, J. R. Sambrano, M. Siu Li, E. Longo, and J. Andrés, Curr. Appl. Phys. **10**, 614 (2010).
[16] Z. Shahri, M. Bazarganipour, and M. Salavati-Niasari, Superlattice. Microst. **63**, 258 (2013).
[17] T. Gholami, M. Salavati-Niasari, M. Bazarganipour, and E. Noori, Superlattice. Microst. **61**, 33 (2013).
[18] M. Salavati-Niasari, B. Shoshtari-Yeganeh, and M. Bazarganipour, Superlattice. Microst. **58**, 20 (2013).
[19] E. Noori, M. Bazarganipour, M. Salavati-Niasari, and T. Gholami, J. Clust Sci. **24**, 1171 (2013).
[20] M. Goudarzi, M. Bazarganipour, and M. Salavati-Niasari, Rsc Adv. **4**, 46517 (2014).
[21] S. Mandizadeh, M. Bazarganipour, and M. Salavati-Niasari, Ceram. Int. **40**, 15685 (2014).
[22] M. Ghaed-Amini, M. Bazarganipour, and M. Salavati-Niasari, J. Ind. Eng. Chem. **21**, 1089 (2015).
[23] S. Gholamrezaei, M. Salavati-Niasari, M. Bazarganipour, M. Panahi-Kalamuei, and S. Bagheri, Adv. Powder Technol. **25**, 1585 (2014).
[24] J. Andrés, L. Gracia, A. F. Gouveia, M. M. Ferrer, and E. Longo, Nanotechnology. **26**, 405703 (2015).
[25] M. M. Ferrer, A. F. Gouveia, L. Gracia, E. Longo, and J. Andrés, Modelling Simul. Mater. Sci. Eng. **24**, 025007 (2016).
[26] S. S. Ding, M. Lei, H. Xiao, G. Liu, Y. C. Zhang, K. Huang, C. Liang, Y. J. Wang, R. Zhang, D. Y. Fan, H. J. Yang, and Y. G. Wang, J. Alloy. Compd. **579**, 549 (2013).
[27] M. Lei, C. X. Ye, S. S. Ding, K. Bi, H. Xiao, Z. B. Sun, D. Y. Fan, H. J. Yang, and Y. G. Wang, J. Alloy. Compd. **639**, 102 (2015).
[28] L. Ma, Y. Sun, P. Gao, Y. Yin, Z. Qin, and B. Zhou, Mater. Lett. **64**, 1235 (2010).
[29] H. Shi, L. Qi, J. Ma, and N. Wu, Adv. Funct. Mater. **15**, 442 (2005).
[30] H. Shi, X. Wang, N. Zhao, L. Qi L, and J. Ma, J. Phys. Chem. B. **110**, 748 (2006).
[31] Z. Luo, H. Li, H. Shu, K. Wang, J. Xia, and Y. Yan, Cryst. Growth Des. **8**, 2275 (2008).
[32] Y. Yin, Z. Gan, Y. Sun, B. Zhou, X. Zhang, D. Zhang, and P. Gao, Mater. Lett. **64**, 789 (2010).
[33] L. K. Bharat, S. H. Lee, and J. S. Yu, Mater. Res. Bull. **53**, 49 (2014).
[34] M. C. Oliveira, L. Gracia, I. C. Nogueira, M. F. C. Gurgel, J. M. R. Mercury, E. Longo, and J. Andrés, Ceram. Inter. **42**, 10913 (2016).

[35] I. C. Nogueira, L. S. Cavalcante, P. F. S. Pereira, M. M. de Jesus, J. M. Rivas Mercury, N. C. Batista, M. S. Li, and E. Longo, J. Appl. Cryst. **46**, 1434 (2013).
[36] O. Gomis, J. A. Sans, R. Lacomba-Perales, D. Errandonea, Y. Meng, J. C. Chervin, and A. Polian, Phys. Rev. B. **86**, 054121 (2012).
[37] H. Zhao, F. Zhang, X. Guo, Q. Zhang, and T. Liu, J. Phys. Chem. Solids **71**, 1639 (2010).
[38] X. Guo, Q. Zhang, T. Liu, M. Song, J. Yin, H. Zhang, and X. Wang, Nucl. Instrum. Meth. B. **267**, 1093 (2009).
[39] V. Nassif, R. E. Carbonio, and J. A. Alonso, J. Solid State Chem. **146**, 266 (1999).
[40] V. Thangadurai, C. Knittlmayer, and W. Weppner, Mater. Sci. Eng. B. **106**, 228 (2004).
[41] A. Phuruangrat, T. Thongtem, and S. Thongtem, Superlattice. Microst. **52**, 78 (2012).
[42] A. Phuruangrat, T. Thongtem, and S. Thongtem, J. Phys. Chem. Solids. **70**, 955 (2009).
[43] T. Thongtem, A. Phuruangrat, and S. Thongtem, Mater. Lett. **62**, 454 (2008).
[44] Z. Luo, H. Li, H. Shu, K. Wang, and J. Xia, Y. Yan, Mater. Chem. Phys. **110**, 17 (2008).
[45] D. Errandonea, L. Gracia, R. Lacomba-Perales, A. Polian, and J. C. Chervin, J. Appl. Phys. **113**, 123510 (2013).
[46] R. Vilaplana, O. Gomis, F. J. Manjón, P. Rodríguez-Hernández, A. Muõoz, D. Errandonea, S. N. Achary, and A. K. Tyag, J. Appl. Phys. **112**, 103510 (2012).
[47] G. Wulff, Z. Kristallogr. Miner. **34**, 449 (1901).
[48] C. Herring, Phys. Rev. **82**, 87 (1981).
[49] J. W. Gibbs, Trans. Conn. Acad. Of Arts Sci. **3**, 108 (1875).
[50] T. Wang, X. Tian, Y. Yang, Y. -W. Li, J. Wang, M. Beller, and H. Jiao, Phys. Chem. Chem. Phys. **18**, 6005 (2016).
[51] Z. Y. Gao, W. Sun, Y. -H. Hu, and X. -W. Liu, T. Nonferr. Metal. Soc. **23**, 2147 (2013).
[52] T. G. Cooper and N. H. de Leeuw, Surf. Sci. **531**, 159 (2003).
[53] P. Mogilevsky, T. A. Parthasarathy, and M. D. Petry, Acta Mater. **52**, 5529 (2004).
[54] H. -Y. Jung and Y. -D. Huh, Crystengcomm. **17**, 1398 (2015).
[55] A. S. Barnard and P. Zapol, Phys. Rev. B. **70**, 235403 (2004).
[56] L. Li, F. Abild-Pedersen, J. Greeley, and J. K. Nørskov, J. Phys. Chem. Lett. **6**, 3797 (2015).
[57] M. Li, Y. Guan, Y. Yin, X. Cui, S. Rong, G. Jin, Y. Hao, and Q. Wu, Superlattice. Microst. **80**, 222 (2015).
[58] E. -K. Ryu and Y. -D. Huh, Bull. Korean Chem. Soc. **29**, 503 (2008).
[59] J. P. Perdew, Int. J. Quantum Chem. **28**, 497 (1985).
[60] A. J. Cohen, P. M.-Sánchez, and W. Yang, Chem. Rev. **112**, 289 (2012).
[61] P. Mori-Sánchez, A. J. Cohen, and W. Yang, Phys. Rev. Lett. **100**, 146401 (2008).
[62] D. Bagayoko, AIP Advances. **4**, 127104 (2014).
[63] H. M. Rietveld, J. Appl. Cryst. **2**, 65 (1969).
[64] A. C. Larson, R. B. V. Dreele, "General Structure Analysis System (Gsas)". Report Laur. Los Alamos National Laboratory: New Mexico Usa; (2004). User Manual.
[65] W. Finger, D. E. Cox, and A. P. Jephcoat, J. Appl. Cryst. **27**, 892 (1994).
[66] P. W. Stephens, J. Appl. Cryst. **32**, 281 (1999).
[67] M. R. D. Bomio, R. L. Tranquilin, F. V. Motta, C. A. Paskocimas, R. M. Nascimento, L. Gracia, J. Andrés, and E. Longo, J. Phys. Chem. C. **117**, 21382 (2013).
[68] V. M. Longo, L. Gracia, D. G. Stroppa, L. S. Cavalcante, M. Orlandi, A. J. Ramirez, E. R. Leite, J. Andrés, A. Beltrán, J. A. Varela, and E. Longo, J. Phys. Chem. C. **115**, 20113 (2011).
[69] G. Botelho, J. Andres, L. Gracia, L. S. Matos, and E. Longo, Chempluschem. **81**, 202 (2016).
[70] M. T. Fabbro, C. Saliby, L. R. Rios, F. A. La Porta, L. E. Gracia, M. S. Li, J. Andrés, L. P. S. Santos, and E. Longo, Sci. Technol. Adv. Mater. **16**, 065002 (2015).
[71] R. Dovesi, V. R. Saunders, C. Roetti, R. Orlando, C. M. Zicovich-Wilson, F. Pascale, B. Civalleri, K. Doll, N. M. Harrison, I. J. Bush, Ph. D'Arco, M. Llunel, M. Causà, and Y. Noël, Crystal 14. University Of Torino: Torino Italy; (2014). User Manual.
[72] A. D. Becke, J. Chem. Phys. **98**, 5648 (1993).
[73] C. T. Lee, W. T. Yang, and R. G. Parr, Phys. Rev. B: Condens. Matter. **37**, 785 (1988).
[74] http://Www.Crystal.Unito.It/Basis_Sets/Oxygen.Html, http://Www.Crystal.Unito.It/Basis_Sets/Molibdenum.Html.
[75] http://Www.Tcm.Phy.Cam.Ac.Uk/~Mdt26/Basis_Sets/Ba_Basis.Txt.
[76] H. J. Monkhorst and J. D. Pack, Phys. Rev. B: Condens. Matter. **13**, 5188 (1976).